I&EC research
Industrial & Engineering Chemistry Research

pubs.acs.org/IECR
Article

Calcium Looping for Thermochemical Storage: Assessment of Intrinsic Reaction Rate and Estimate of Kinetic/Transport Parameters for Synthetic CaO/Mayenite Particles from TGA Data

Silvia Lo Conte, Maria Anna Murmura,* Francesca Fratini, Stefano Cerbelli, Michela Lanchi, Annarita Spadoni, Luca Turchetti, and Maria Cristina Annesini

Cite This: *Ind. Eng. Chem. Res.* 2023, 62, 16647−16659

ABSTRACT: Mayenite-supported CaO represents an affordable and safety-compliant candidate material for thermochemical storage processes. We here analyze the thermogravimetric analysis (TGA) performance of synthetic CaO/mayenite micrometric powder under carbonatation/calcination looping and develop a model to interpret and analyze the experimental results. In the experimental campaign, calcination is run at 900 °C, while the carbonatation temperature is varied between 600 and 800 °C. For the carbonatation reaction, a generalized shrinking core model assuming a thermodynamically consistent first-order kinetic and a conversion-dependent diffusivity of CO_2 inside the porous $CaCO_3$ layer is validated through TGA carbonatation tests conducted with CO_2/N_2 mixtures at different compositions. Interestingly, the kinetic constant of this reaction is found to be relatively insensitive to the temperature in the interval considered. In contrast, diffusion-limited regimes are never found for the calcination reaction so that this phase of the cycle can be predicted based on a single kinetic constant of the heterogeneous reaction. This constant is found to follow the typical Arrhenius-type dependence on temperature. Sizably different kinetic and transport parameters are obtained in the first carbonation performed on virgin CaO/mayenite particles with respect to those associated with subsequent cycles. When different parameters are afforded for the first and following cycles, the shrinking core model proposed closely predicts the TGA data over five $CaO/CaCO_3$ cycles. The results found constitute an essential preliminary piece of information for designing equipment geometry and operating conditions of industrial-scale reactors. In this respect, knowledge of the parameters defining the intrinsic reaction rates and diffusive transport is essential in defining the optimal conversion of the material associated with minimal looping time.

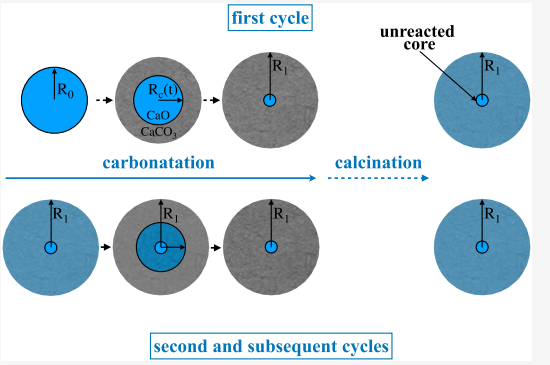

INTRODUCTION

According to the International Energy Agency (IEA), renewable electricity generation increased by almost 7% in 2021, with wind and solar photovoltaic technologies together accounting for almost 90% of this growth.[1] Concentrated solar power (CSP) plants, which concentrate sunlight to convert it into high-temperature thermal energy for direct or indirect operation of heat engines and electricity generators, are relatively recent developments. In 2022, the total global installed capacity of CSP was approximately 6 GW. However, the IEA expects it to grow significantly in the years to come, reaching approximately 900 GW by 2050.[2,3] This significant growth in renewable energy capacity highlights the need for energy storage technologies to allow efficient integration of these intermittent sources into the grid. Energy storage may also play an important role in the industrial sector, where waste heat is currently underutilized.[4−6] This may be due to technical and economic shortcomings associated with conventional heat recovery methods as well as temporal or geographical mismatch between the energy released and its demand. By enabling the storage of thermal energy for later use, thermal energy storage (TES) can help not only to address the challenges posed by intermittent renewable energy sources, especially solar energy, but also to improve the efficiency of industrial processes.

Thermal energy can be stored as sensible heat, latent heat, chemical reaction heat, or combinations thereof. Sensible TES use materials with high specific heat[7] (131−4187 J/kg K) to store/release the energy by heating/cooling processes. These systems are simple, reliable, and cheap, but their energy storage

Received: May 31, 2023
Revised: September 5, 2023
Accepted: September 5, 2023
Published: September 19, 2023

https://doi.org/10.1021/acs.iecr.3c01820
Ind. Eng. Chem. Res. 2023, 62, 16647−16659

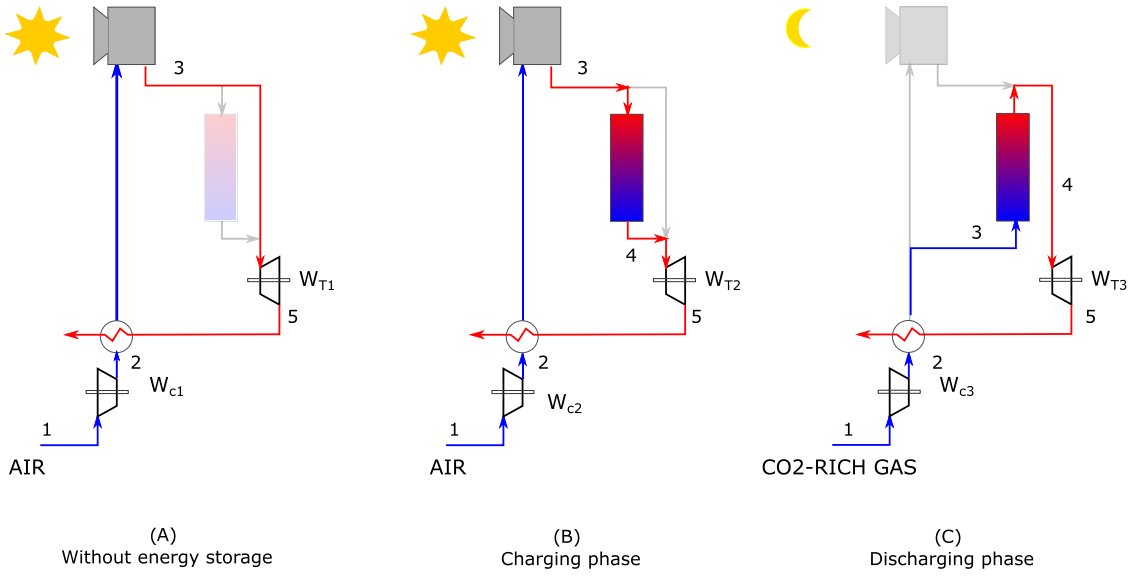

Figure 1. Integration of thermochemical energy storage systems with concentrated solar power plants.

density is low[8] (~60 kWh/m^3). Melting/solidification latent heat TES systems have the potential to reach higher efficiencies than sensible TES systems due to their nearly isothermal process conditions and promise higher energy densities[8,9] (~100 kWh/m^3). However, despite the large number of phase-change materials[10] proposed, the efficiency of latent heat TES systems is limited by low charge/discharge rates due to the low thermal conductivity of most materials[7] (<0.5 W/m K), fouling of heat transfer surfaces by solid deposition, and volumetric expansion[9] during the phase change. Thermochemical energy storage systems (TCES) are based upon reversible gas−solid reactions, characterized by high enthalpy changes, to store and release energy through a cyclic process. These systems have the potential to provide higher operating temperatures and energy densities[11] (~600 kWh/m^3) and negligible heat loss over longer periods compared to both sensible and latent heat TES technologies. Important requirements for TCES materials include reversibility of the chemical reaction, temperature compatibility with power cycles or coupled processes, high reaction rates of forward and backward reactions, absence of side reactions, high specific enthalpy of reaction, high specific heat capacity, long-term cycling stability, environmental compatibility, nontoxicity, and low cost. A generalized scheme showing the way thermochemical energy storage systems may be coupled to CSP plants is shown in Figure 1. A more detailed discussion of such integration is reported in Lanchi et al.[12]

Among several chemical looping alternatives (hydrides, metal oxides, and carbonate salts[13,14]), the calcium looping (CaL) process has attracted great interest as a promising system for TCES since it displays several advantages such as low cost, nontoxicity, high reaction temperature for the exothermic reaction (650−850 °C), low hysteresis, and high energy density[11] (~692 kWh m^3). The CaL process is based on the reversible calcination of $CaCO_3$ into CaO

$$CaCO_3 \rightleftharpoons CaO + CO_2 \quad (1)$$

The CaL process exhibits two significant drawbacks that penalize its large-scale implementation, namely, the incomplete conversion of CaO and its progressive deactivation along the successive carbonation/calcination cycles.[15,16] Many authors have highlighted that the carbonation reaction proceeds quickly up to a critical conversion (kinetics-controlled regime), above which a sharp reduction in the reaction rate is observed[17−21] (diffusion-limited regime). In particular, Bhatia and Perlmutter[19,20] have shown that, when working with CaO obtained by limestone calcination, the transition from the fast reaction phase to the slow phase occurs at a critical conversion. According to their random pore model, since the conversion involves the formation of a compound ($CaCO_3$) with a molar volume (36.9 cm^3 mol^{-1}) greater than the molar volume of the reactant (CaO, 16.7 cm^3 mol^{-1}), the conversion results in a reduction of the porosity of the structure. The authors identified the critical conversion as that in which the smaller pores, which are attributed to provide most of the reaction surface areas, are completely occluded. According to this interpretation, in the slow phase of the reaction, carbonatation is possible only in larger pores with a low surface area. Similarly, Stendardo and Foscolo[22] have employed a multigrain shrinking core model, in which the carbonatation reaction is considered to proceed through an initial, fast kinetically controlled step, followed by a slower step in which the process is limited by a conversion-dependent diffusion of CO_2 through the ash layer.

The other main issue associated with the CaL process is the loss of reactivity of CaO obtained from natural sources such as limestone, which undergoes a rapid decline in its ability to react with CO_2 upon repeated cycles of calcination and carbonation. This characteristic of limestone-derived CaO is well documented[17,23,24] and is generally attributed to the extensive sintering and loss of surface area that occurs at the high temperature and high CO_2 partial pressure[25,26] required. In addition, it has been noted that when calcination is carried out in an inert gas, during the subsequent carbonatation, a blocking layer of $CaCO_3$ forms rapidly on the surface of the CaO particles. This pore-plugging layer significantly hinders the diffusion of CO_2 molecules and hence prevents complete conversion.[18,27]

In the last two decades, many researchers worldwide have focused on the issue of material deactivation in CaO-based materials. The most commonly used approaches include (i) incorporating CaO particles into various inert supports;[28−33]

https://doi.org/10.1021/acs.iecr.3c01820
Ind. Eng. Chem. Res. 2023, 62, 16647−16659

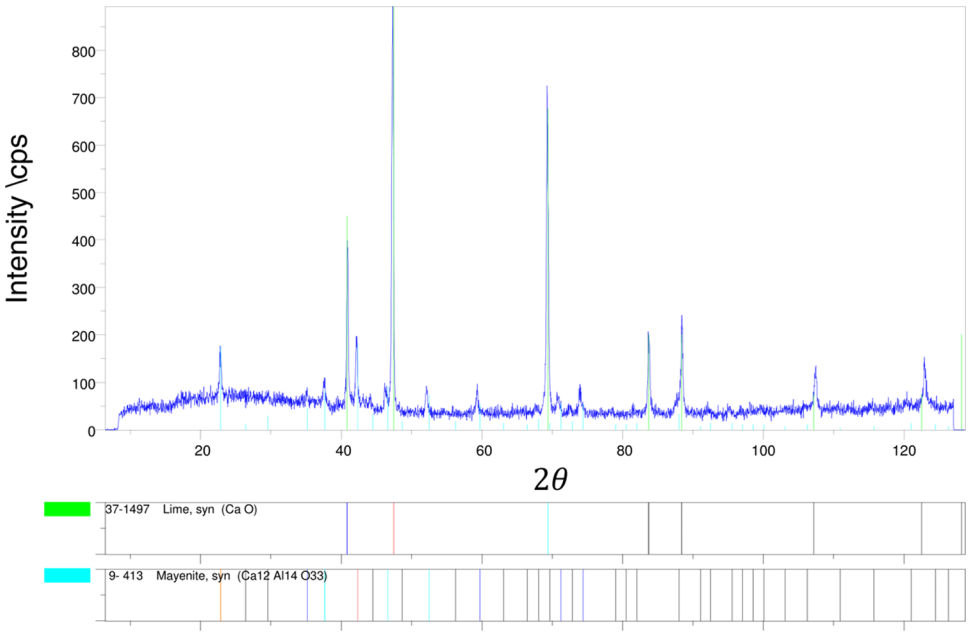

Figure 2. X-ray diffraction spectra of CaO/mayenite synthesized at the laboratories of the ENEA Casaccia Research Center.

(ii) hydration treatment;[34−36] (iii) using sintering-resistant calcium precursors;[37,38] and (iv) modifying natural calcium minerals by ball milling or acidification.[39,40] While most of these approaches have demonstrated some success in enhancing the performance of CaO-based materials for TES, incorporating CaO particles into inert supports is the most extensively studied and effective approach to solving the loss-in-reactivity issue. Basically, adding inert materials that are resistant to sintering can improve the stability of the material during usage cycles by reducing the loss of active sites. However, adding these materials also leads to a reduction in the energy storage density per unit mass of the composite material. Therefore, it is necessary to strike a balance between the stability and energy storage density by properly adjusting the amount of added inert material. To date, over a dozen inert supports have been employed and investigated to improve the cyclic performance of CaO-based materials, comprising binary oxides of cobalt, iron, and copper, as well as additives[41,42] based on yttrium and aluminum.

Given the good performance exhibited by synthetic calcium-based materials containing aluminum, in this work, we focus on CaO-based systems supported on mayenite/$CaCO_3$, henceforth referred to as CaO−mayenite/$CaCO_3$. Compared to natural sorbents like dolomite or limestone, synthetic mayenite ($Ca_{12}Al_{14}O_{33}$) is not only more expensive (about four times higher) but also much more durable,[43] with less than a 10% reduction in its CO_2 sorption capacity after 50 cycles, compared to a 40% reduction for natural sorbents. Although this material has been extensively researched for CO_2 capture applications,[44] there are still several aspects that need to be investigated to determine its suitability for heat storage applications. Previous studies on the CaO/mayenite system have mainly focused on factors affecting reactivity, such as preparation method, calcium and aluminum precursors, CaO/mayenite ratio, residence time, particle size, carbonatation temperature, calcination temperature, and stability under ambient air[32] conditions.

In this work, an analysis and modeling activity was carried out for the CaO−mayenite/$CaCO_3$ system, focusing on the system behavior during usage cycles. The model employed is a shrinking core, multigrain model similar to the one previously employed in the work of Stendardo and Foscolo,[22] but the analysis was extended to consider the effect of different CO_2 concentrations in the gas employed in the carbonatation reaction. In addition, the different behavior before the first and subsequent carbonatation/calcination cycles was investigated.

The reactive material consisting of CaO supported on an inert matrix of mayenite was synthesized at the laboratories of the ENEA Casaccia Research Center. The powder obtained from the synthesis was then tested in a thermogravimetric analyzer (TGA) under carbonatation/calcination looping, and the results confirmed that the addition of mayenite effectively stabilizes the material, ensuring high and sustained conversion over time.[32,33] The kinetic characterization of the material for the carbonation and calcination phases was then carried out. The powder was assumed to be made of distinct CaO/$CaCO_3$ and mayenite grains, and the kinetic behavior of the single CaO/$CaCO_3$ grain was described using a generalized shrinking core model. The material was tested in TGA enforcing three different protocols described in detail in the next section: changing the calcination or carbonatation operating temperature or the CO_2 molar fraction adopted during the carbonatation phase. The experimental results allowed for the assessment of the intrinsic reaction rate and estimation of kinetic/transport parameters.

MATERIALS AND METHODS

Experimental Section. For the reasons discussed above, mayenite-supported CaO/$CaCO_3$ was selected as the thermochemical looping material for the present study. For reproducibility issues and better performance over cycling, the material was synthesized in-house. A two-step synthesis method was adopted, which is a modification of the method previously described by Di Giuliano et al.[45] First, 1.25 g of mayenite was prepared using 4.733 g of aluminum nitrate nonahydrate ($Al(NO_3)_3{\cdot}9H_20$, Acros Organics) and 0.607 g of calcium oxide (CaO, Acros Organics) in a stoichiometric ratio to obtain 12 CaO·7 Al_2O_3. Mixed solid powders were added to

https://doi.org/10.1021/acs.iecr.3c01820
Ind. Eng. Chem. Res. 2023, 62, 16647−16659

11 mL of isopropyl alcohol (99.5%, Sigma-Aldrich) and 83 mL of deionized water and homogenized at 70 °C for 1 h. The solvent was then evaporated at 150 °C for 1 h, and the resulting sample was transferred to a kiln for calcination. The calcination procedure was as follows: (i) from 50 to 150 °C at a heating rate of 5 °C/min and dwell at 150 °C for 1 h; (ii) from 150 to 500 °C at a heating rate for 5 °C/min and dwell for 1 h; and (iii) from 500 to 1000 °C at a heating rate of 5 °C/min and dwell for 1 h. The recipe for mayenite synthesis was taken from the previous work by Li et al.,[46] but the calcination temperature was selected according to the findings previously published by some of the same authors of the present work.[47] In the second step, a sample of 0.5 g of synthetic mayenite thus obtained was mixed with 1.5 g of CaO in 4.4 mL of isopropyl alcohol and 33.2 mL of deionized water. The mixture was then stirred over a heating plate at 70 °C, and the calcination procedure was repeated (see Di Giuliano et al.[48] for details on the mixing procedure). The quantities were chosen so that the final sample contained 75% of the weight of CaO. The material was then crushed to a fine powder with a diameter of approximately 0.5 mm. XRD spectra were determined for the sample, which showed a homogeneous distribution of mayenite and CaO phases, as can be gathered from Figure 2. Preliminary tests showed that this procedure provides a high-performing material in terms of both reactivity and stability over carbonatation/calcination cycling (not shown for the sake of brevity). An attempt was also made to increase the energy density of the material by increasing the weight of CaO from 75 to 91.5%. Figure 3 shows the stability

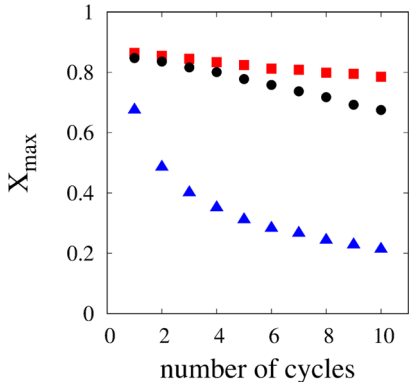

Figure 3. Maximum carbonation conversion over cycling. Squares: 75% CaO 25% mayenite material. Circles: 91.5% CaO 8.5% mayenite. Triangles: natural limestone.[23]

of conversion over cycling in terms of the maximum conversion at the end of each carbonatation step. The maximum conversion of the 75% CaO sample (filled squares) is maintained above 80% during the first 10 cycles, whereas the 91.5% sample shows a relatively rapid deterioration of the performance. For comparison, the triangular symbols show the behavior of a natural limestone, whose performance is hardly compatible with an industrial use of the material. Notwithstanding the larger CO_2 uptake due to the larger amount of CaO, the sample showed a rapid deterioration of the performance over cycling in that the smaller amount of mayenite present was less effective in preventing synthesization phenomena. For these reasons, only 75% of CaO material obtained through the impregnation/calcination method is next considered.

In order to single out the effects of the diffusion of CO_2 through the $CaCO_3$ layer on the overall carbonatation kinetics, thermogravimetric analyses were conducted. The experimental tests were conducted on a TGA/DSC apparatus (Mettler Toledo) at ENEA Casaccia laboratories on a 75% CaO material hosted in a 70 μL alumina crucible. Twenty-five mg of sample was loaded on the crucible, and the material was first heated from 50 to 900 °C and pretreated by calcination at this temperature under a 50 N mL/min pure N_2 flow for 1 h to ensure complete carbonatation and the removal of any adsorbed humidity. At the end of this pretreatment, the mass of the sample varied between 18 and 25 mg. The sample was then brought to 700 °C under a pure nitrogen flow. Starting from this condition, two groups of experimental tests were conducted. In the first group, a single-carbonatation reaction was conducted by feeding the TGA apparatus with CO_2/N_2 gas mixtures at different compositions for 2 h. Similar experimental runs were also conducted for T = 600 °C. In the second group, the carbonatation was conducted under a pure CO_2 current and the temperature was kept fixed at 700 or 800 °C.

Then, in order to assess the response of the material to $CaO/CaCO_3$ looping, tailored TGA experiments were conducted. As for the previous tests, the sample was pretreated by calcination at 900 °C under N_2 for 1 h. The sample was then brought to 700 °C still under a pure nitrogen flow. Starting from this condition, five carbonatation/calcination cycles were enforced by switching the gas feed from pure N_2 to pure CO_2. During the calcination reaction, the nitrogen temperature varied from 700 to 900 °C, keeping the temperature fixed at 900 °C for 10 min, whereas, during the carbonatation, the carbon dioxide temperature was kept fixed at 700 °C for 20 min.

Experimental runs were conducted for three values, T = 600, 700, and 800 °C, of the carbonatation temperature. In all cases, the temperature of the calcination reaction was kept constant to 900 °C. All tests were run in duplicate. Henceforth, we refer to these experimental runs as P600A, P700A, and P800A (P600B, P700B, and P800B for the duplicates) where PyyyA and PyyyB denote protocols with carbonatation temperature equal to yyy °C. Starting from the 75% CaO sample, and defining the conversion $X_{CaO}(t)$ as the mass of CaO converted into $CaCO_3$ to the initial CaO mass, one obtains the relationship between $X_{CaO}(t)$ and the total mass of the sample $m(t)$

$$X_{CaO}(t) = \frac{1}{0.75}\frac{m(t)/m(0) - 1}{W_{CaCO_3}/W_{CaO} - 1} \quad (2)$$

W_{CaCO_3} and W_{CaO} are the molecular weights of calcium carbonate and calcium oxide, respectively. To provide an example, Figure 4 shows the conversion curves for the test P800A. Beyond the fact that a slight (linear) decrease of the maximum conversion is already apparent over the first five cycles, one observes how the first carbonatation shows a qualitatively different behavior of conversion vs time when compared to the subsequent ones. This clearly suggests that the first carbonatation occurs via a different mechanism, a circumstance that must be taken into consideration when developing a model to interpret the experimental trends.

Tailored experiments were also implemented to single out the kinetics of the calcination reaction and validate the transport-reaction model. In this case, a two-cycle protocol was

https://doi.org/10.1021/acs.iecr.3c01820
Ind. Eng. Chem. Res. 2023, 62, 16647−16659

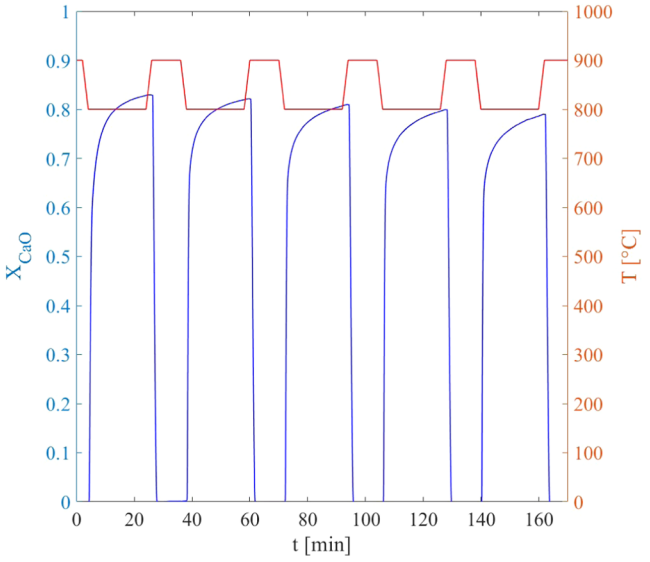

Figure 4. Conversion (blue) and temperature (red) vs time for the TGA test P800A, where the carbonatation and calcination reactions are conducted at 800 and 900 °C, respectively.

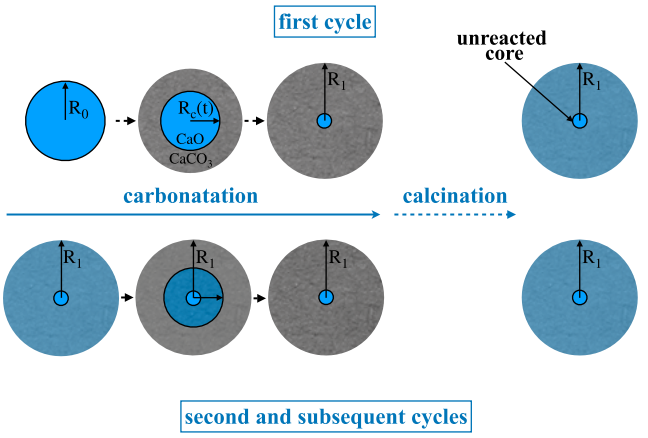

Figure 5. Shrinking core model for the carbonatation/calcination cycle. A difference is allowed for the first cycle, where the initial calcium oxide grain of radius R_0, supposedly nonporous, is converted to a grain of $CaCO_3$, whose radius R_1 is larger than R_0 (see the main text for details). After the first carbonatation, the external grain radius is assumed constant for all of the subsequent calcination/carbonatation cycles.

enforced. Here, the calcination temperature was controlled by feeding the TGA apparatus with pure nitrogen at T = 900, 850, 800, and 750 °C for 15 min, and the carbonatation was carried out at a fixed temperature of 700 °C for 20 min.

Modeling. The conversion/time curves determined from the TGA experiments are next interpreted through a generalized shrinking core model. In developing this model, we assume that the generic particle is composed of CaO and mayenite (inert) grains organized in a macroporous structure that, owing to the large pore size, offers no resistance to either mass or heat transport. Therefore, at any time instant, the local gas temperature and composition at the external surface of the grains are identical to those outside the particle embedding the grains. This much established, we also assume that the individual CaO grain is initially a compact nonporous spherically shaped solid, with radius R_0, as represented in Figure 5. As the carbonatation reaction advances during the first cycle, a layer of $CaCO_3$ is formed, which sticks to the unreacted core (see Figure 5). In principle, one would expect that during the first carbonatation, the $CaCO_3$ layer formed should possess some degree of porosity, so that transport toward the reaction surface is made possible. On the other hand, the diffusion coefficient for this phase of the cycle as obtained by best fit of TGA data (see the Results section) is compatible with that of a gaseous molecule diffusing through a solid crystal. For this reason, we assume that the porosity of the $CaCO_3$ grain formed from the virgin CaO is negligible. Note that during this first cycle, the external grain volume is not preserved because the molar volume of $CaCO_3$ is larger than that of CaO. As a result, the grain radius, R_1, at the final carbonatation conversion, say $X^1_{Cao,max}$, is larger than the initial grain radius R_0. Next, when $CaCO_3$ is subjected to calcination, one can assume that the external grain volume remains constant and that the weight loss due to the CO_2 released changes only the internal porosity of the grain. The TGA data show that at 900 °C the calcination reaction swiftly brings back the conversion to zero. As discussed in the previous section, specific experiments were devised to determine the dependence of the overall time scale of this reaction at different temperatures. Figure 6 shows the relative weight loss during the calcination phase in the first of the two-cycle protocol. The

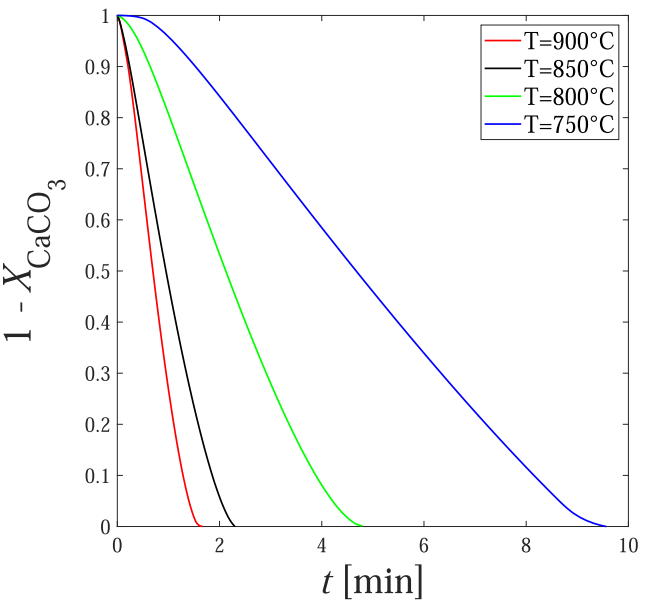

Figure 6. Weight loss for the calcination reaction in the first of a two-cycle protocol at different temperatures in TGA. In all cases, the carbonatation reaction closing the cycle was carried out at T = 700 °C.

results are reported in terms of $(1 - X_{CaCO_3})$, where X_{CaCO_3} is the conversion of carbonate, defined as

$$X_{CaCO_3} = \frac{1}{m^0_{CaCO_3}/m(0)} \frac{m(t)/m(0) - 1}{W_{CaO}/W_{CaCO_3} - 1} \quad (3)$$

In the above equation, $m(0)$ and $m^0_{CaCO_3}$ are the mass of the sample and of $CaCO_3$, respectively, at the beginning of the calcination step. Both of these values depend on the degree of conversion achieved in the previous carbonatation step.

https://doi.org/10.1021/acs.iecr.3c01820
Ind. Eng. Chem. Res. 2023, 62, 16647−16659

As can be gathered from the data, the overall calcination time ranges from order 10 min at the lowest temperature to order 1 min at T = 900 °C. Besides, it is clear that the calcination reaction does not suffer from diffusional limitations in that the advancement of the reaction creates an overpressure inside the grain pores. In turn, the internal pressure gradient generates a convective flow of the gas phase toward the external grain surface, therefore providing an effective transport mechanism for CO_2 release that proves way more efficient than molecular (i.e., diffusive) transport. Then, it is expected that the calcination reaction will be controlled exclusively by the intrinsic reaction kinetics. Following the above observations, we next assume that, after the first carbonation, the external grain radius is constant throughout the cycles and equal to R_1. Therefore, considering the difference in molar volume between $CaCO_3$ and CaO, we also assume that the CaO grain produced has a certain degree of porosity. The relationship between the initial radius, R_0, of the CaO grain and R_1 depends on the ratio $Z = \nu_{CaCO_3}/\nu_{CaO}$ between the molar volume ν_{CaCO_3} of calcium carbonate to that of calcium oxide, ν_{CaO}, and on the maximum conversion $X^{(1)}_{CaO,max}$ as

$$R_1 = R_0(1 - X^{(1)}_{CaO,max} + ZX^{(1)}_{CaO,max})^{1/3} \quad (4)$$

Next, a generalized shrinking core model is enforced for the carbonatation reaction. The effective kinetics of the calcination reaction is then derived by the same model by assuming that this reaction is exclusively controlled by the intrinsic reaction kinetics, thus, disregarding diffusional limitations.

The shrinking core model for the carbonatation yielding the conversion $X_{CaO}(t)$ is constructed based on the following assumptions:

1. The heterogeneous reaction

$$CO_{2(g)} + CaO_{(s)} \rightleftharpoons CaCO_{3(s)} \quad (5)$$

mainly occurs at the surface of the unreacted core and is characterized by the first-order surface kinetics

$$(-r_{CaO}) = k_s(c^{(s)}_{CO_2} - c_{CO_2,eq}) \quad (6)$$

where $(-r_{CaO})$ represents the moles of CO_2 converted per unit reaction surface area per unit time, and where $c^{(s)}_{CO_2}$ and $c_{CO_2,eq}$ denote the carbon dioxide concentration at the surface of the unreacted core and the equilibrium concentration of the carbonatation reaction at the local surface temperature, respectively. Note that, because the reaction is heterogeneous, the kinetic constant k_s has the physical dimensions of a velocity (e.g., cm/s).

2. The equilibrium concentration $c_{CO_2,eq}$ is estimated by assuming the ideal behavior of the gaseous mixture as $c_{CO_2,eq} = P_{CO_2,eq}/\mathcal{R}T$, $\mathcal{R}$ being the universal gas constant. For the dependence of equilibrium pressure vs temperature, we use the correlation by Garcia-Labriano[49] et al.

$$P_{CO_2,eq} = 4.137 \times 10^7 \exp(-20474/T) \quad (7)$$

where P is expressed in atm and T in K.

3. Quasi-steady-state conditions are assumed, where the CO_2 hold-up in the pore volume is neglected.

4. Following previous studies,[22] a conversion-dependent effective diffusion coefficient, say $D_p(X_{CaO})$, in the porous layer of $CaCO_3$ must be allowed to account for pore obstruction due to the residual advancement of the carbonatation in the converted layer. More specifically, in the present study, an empirical two-parameter expression of the type

$$D_p(X_{CaO}) = D^{(0)}_p X^{-b}_{CaO} \quad (8)$$

was proposed, where the effective diffusivity at unit CaO conversion, $D^{(0)}_p$, and the exponent b are next regarded as adjustable parameters.

By the qualitative picture depicted in Figure 5, the enforcement of the shrinking core approach to the first carbonatation cycle must take into account the fact that the external grain radius continuously varies as the initially nonporous grain is converted. One obtains the final expression

$$\frac{dX_{CaO}}{dt} = \frac{3(1 - X_{CaO})^{2/3}}{\tau_k + \tau_D g(X_{CaO})} \quad (9)$$

where

$$\tau_k = \frac{1}{\nu_{CaO}} \frac{R_0}{k_s(c_{CO_2} - c_{CO_2,eq})} \quad (10)$$

is the characteristic time of the surface reaction (c_{CO_2} being the carbon dioxide concentration of the gas outside the grain)

$$\tau_D = \frac{1}{\nu_{CaO}} \frac{R_0^2}{D_p(c_{CO_2} - c_{CO_2,eq})} \quad (11)$$

is the characteristic time for the diffusion of CO_2 through the porous layer of $CaCO_3$, and where the function $g(X_{CaO})$ is given by

$$g(X_{CaO}) = \sqrt[3]{1 - X_{CaO}}\left(1 - \sqrt{[}3]\frac{1 - X_{CaO}}{1 - X_{CaO} + ZX_{CaO}}\right) \quad (12)$$

In the second and subsequent cycles, the same expressions as above hold true for τ_k and τ_D, with R_1 given by eq 4 in place of R_0, whereas the function g(X) simplifies to

$$g(X_{CaO}) = \sqrt[3]{1 - X_{CaO}}(1 - \sqrt{[}3]1 - X_{CaO}) \quad (13)$$

Note that in all cases $g(X_{CaO}) \rightarrow 1$ as $X_{CaO} \rightarrow 0$; thus, it is expected that $dX_{CaO}/dt \simeq 3(1 - X_{CaO})^{2/3}/\tau_k$ at the initial stage of the carbonatation. Also, by assuming ideal behavior for the gas phase, both c_{CO_2} and $c_{CO_2,eq}$ can be computed if the composition, the total pressure, and the temperature of the gas are known. These observations are next used to derive the characteristic time for the reaction, from which, in turn, the kinetic constant characterizing the intrinsic reaction rate can be obtained.

As regards the characteristic calcination time, henceforth referred to as τ_{calc}, one could in principle enforce the same shrinking core approach used for the carbonatation. However, an order-of-magnitude analysis (not discussed for the sake of brevity) suggests that the characteristic time of diffusion of CO_2 through the pores of the CaO layer formed during the advancement of the reaction is well below 1 s. This result is consistent with previous studies,[50,51] which show that diffusional limitations become relevant only for larger grains, i.e., radius of the order of mm. Besides, the data represented in Figure 6 clearly indicate that, for temperatures above 800 °C, the overall characteristic reaction time is of the order of

https://doi.org/10.1021/acs.iecr.3c01820
Ind. Eng. Chem. Res. 2023, 62, 16647−16659

minutes, i.e., almost 10 min lower than the carbonatation step. By this observation, one can assume that a shrinking core model, which only takes the intrinsic reaction kinetics into account, can be used for interpreting the calcination reaction

$$(-r_{CaCO_3}) = k_s'\left(1 - \frac{c_{CO_2}}{c_{CO_{2,eq}}}\right) \quad (14)$$

By this approach, the conversion, $X_{CaCO_3}(t)$, of calcium carbonate during the calcination reaction only depends on the kinetic parameter k_s' as

$$X_{CaCO_3}(t) = 1 - \left(1 - \frac{k_s' \nu_{CaCO_3}}{R_1} t\right)^3 \quad (15)$$

where ν_{CaCO_3} is the intrinsic molar volume of calcium carbonate. Here, $X_{CaCO_3} = (1 - X_{CaO})/X_{CaO,max}$, $X_{CaO,max}$ being the maximum carbonatation conversion of the generic cycle. The characteristic time scale of the calcination reaction, τ_{calc}, can be therefore defined as

$$\tau_{calc} = \frac{R_1}{\nu_{CaCO_3} k_s'} \quad (16)$$

RESULTS

As discussed above, the results next reported refer to a 75% CaO sample obtained through a calcination/impregnation procedure. The experiments were divided into three groups.

In the first group, mainly aimed at validating the kinetic expression for the heterogeneous surface carbonatation reaction expressed by eq 6, a single-carbonatation reaction was conducted at 600, 700, and 800 °C by feeding the TGA apparatus with CO_2/N_2 gas mixtures at different compositions. Table 1 summarizes the tests carried out at different temperatures and compositions of the gas fed to the TGA apparatus. In the second group of experiments, the five-cycle protocol described in Figure 4 was enforced. Here, pure CO_2 and N_2 were used for the carbonation and calcination reactions, respectively. In Figure 4, the difference between the first carbonation and the subsequent ones is clearly visible. Following this observation, the characteristic time τ_k and the parameters D_p^0 and b entering eq 8 were computed separately by best fit of the TGA data for the first group of experiments, i.e., single carbonatation, and for the second group, consisting of the second cycle and the subsequent ones.

Table 1. Synoptic Scheme of the Conditions for Carbonation at Different Compositions of the Gas Feed[a]

T	y_{CO_2}	duration	X_{CaO}^{max} %	n_{test}	Δc_{CO_2}
600	0.05	115	77.7/81.5	2	0.66
600	0.1	115	80.0	1	1.36
600	0.15	115	80.0/81.6	2	2.05
700	0.05	115	77.7−81.5	2	0.66
700	0.07	110	75.0	1	0.50
700	0.1	11	82.0	1	0.87
700	0.15	115	86.0	1	1.50
700	1	50	87	1	12.14
800	1	50	82	1	8.92

[a]Units for temperature, test duration, and concentration are °C, min, and mol/m^3, respectively. All experiments were run at atmospheric pressure.

In the third group of experiments, a two-cycle carbonatation/calcination protocol was enforced as described in the Experimental Section. These experiments were aimed exclusively at determining the values of the kinetic constant k_s' of the calcination reaction.

Estimate of τ_k and Validation of the Kinetic Expression. As discussed in the previous section, the fact that $g(X_{CaO}) \to 0$ as $X_{CaO} \to 0$ implies that at the beginning of the carbonatation reaction, the rate of conversion should obey the relationship

$$\frac{dX_{CaO}}{dt} = (3/\tau_k)(1 - X_{CaO})^{2/3} \text{ for } 0 \le t \le t_k \quad (17)$$

where $(0, t_k)$ denotes the time range in which kinetic control holds true. Equation 17 can be integrated by inspection to obtain the relationship between conversion and time

$$1 - (1 - X_{CaO}(t))^{1/3} = t/\tau_k \quad (18)$$

Thus, from eq 18, one expects that for any given condition of the TGA test (i.e., for fixed composition and temperature of the gas feed), there exists a time interval $0 \le t \le t_k$ where the function $1 - (1 - X_{CaO}(t))^{1/3}$ is represented by a straight line through the origin with slope $1/\tau_k$. Figure 7 shows the behavior of this function at the early stages of the carbonatation at T = 600 °C (panel (a)) and T = 700 °C (panel (b)).

As can be gathered from the data, an interval $(0, t_k)$ where the scaling is linear can unambiguously be identified in all cases, with the value of t_k depending on the specific composition/temperature conditions. The values of τ_k derived from this approach are summarized in Table 2 for the first cycle and in Table 3 for the subsequent ones. Note that, for fixed operating conditions, sizably different values of τ_k are obtained for the carbonatation performed on virgin CaO/mayenite particles with respect to those associated with subsequent cycles. With regard to the effect of feed composition, the comparison of data at different CO_2 concentrations highlights that within the linearity range, t_k decreases at increasing values of y_{CO_2}. From the values τ_k reported in Table 2, the kinetic constant for the first carbonatation can be computed at any given temperature from the knowledge of the concentration difference $\Delta c_{CO_2} = c_{CO_2} - c_{CO_2,eq}$ through eq 10. The subsequent cycle kinetic constants can be similarly estimated from the value reported in Table 3. However, in this case, the value of the apparent CaO molar volume, ν_{CaO} in eq 10, must be corrected to account for the formation of the porous structure, as explained in the Modeling section. Therefore, the kinetic constant computed for the subsequent cycles is higher with respect to the one of the first carbonatation. In all cases, it is worth observing that the linear dependence of $1/\tau_k$ on Δc_{CO_2} is ultimately a consequence of the kinetic expression postulated in eq 6 for the heterogeneous surface reaction. Conversely, a linear scaling of $1/\tau_k$ as a function of Δc_{CO_2} derived by the approach discussed above from TGA data at a constant temperature and variable gas composition provides a direct validation of the intrinsic carbonatation kinetics that was assumed for developing the shrinking core model. Figure 8 depicts the experimentally determined values of $1/\tau_k$ vs Δc_{CO_2}, determined

https://doi.org/10.1021/acs.iecr.3c01820
Ind. Eng. Chem. Res. 2023, 62, 16647−16659

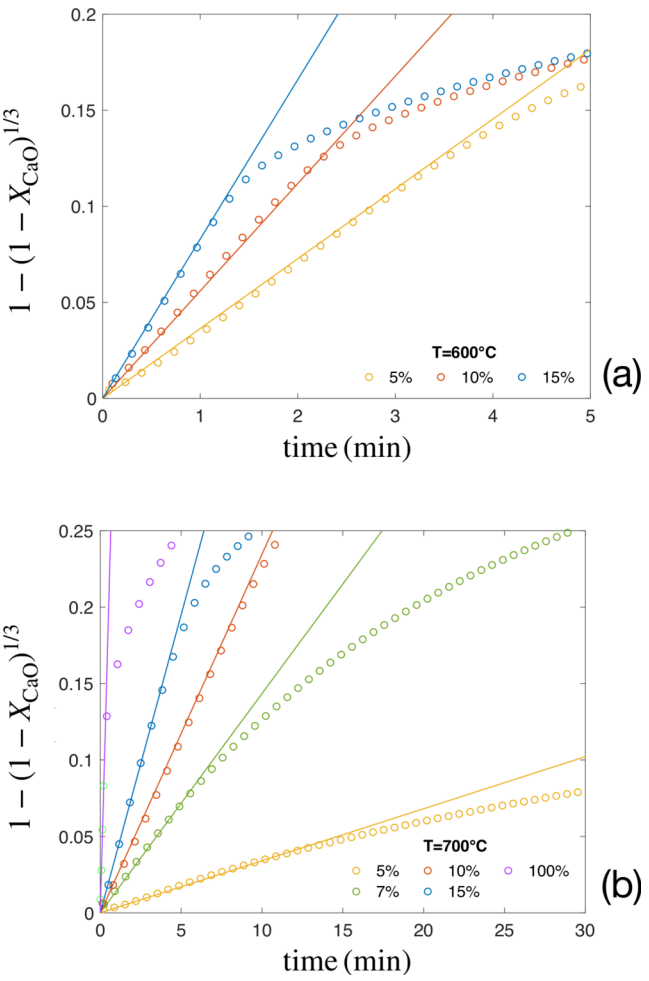

Figure 7. Estimate of the characteristic time τ_k of the first carbonatation reaction from the scaling of the function $1 - (1 - X_{CaO}(t))^{1/3}$ for different compositions of the CO_2/N_2 gas mixture fed at the TGA apparatus at T = 600 °C (panel (a)) and T = 700 °C (panel (b)). The slope of the linear approximation to the curves in the figure yields the inverse time $1/\tau_k$. Note that the experimental data were collected every 2 s, but here the values were reported every 10 s for the sake of graphics clarity.

Table 2. Values of τ_k for the First Carbonatation (Expressed in s) Estimated from the Linear Scaling of the Data Depicted in Figure 7[a]

y_{CO_2}	τ_k (600 °C)	τ_k (700 °C)	τ_k (800 °C)
0.05	1616−1650	13,902−23,784	
0.07		4183	
0.10	1073	2558	
0.15	723	1540	
1		155	232

[a]Multiple values refer to tests performed in duplicate.

from the single-carbonatation experiments, where the linear scaling is well recognizable for both sets of isothermal data at T = 600 °C (green symbols) and T = 700 °C (purple). Note that the slope of the best interpolating straight line should depend only on temperature. Besides, even the complete set of data performed at different temperatures appears to scale linearly, thus suggesting that the kinetic constant k_s of the first-order reaction can be approximately considered constant in the range of 600/800 °C. The same goes for the second and subsequent

Table 3. Values of τ_k (Expressed in s) Are Estimated from the Linear Scaling of the TGA Data of the Five-Cycle Protocol[a]

	2nd cycle	3rd cycle	4th cycle	5th cycle
P600A	74.1	74.2	74.9	74.7
P600B	77.3	77.5	78.8	84.3
	2nd cycle	3rd cycle	4th cycle	5th cycle
P700A	84.8	84.8	83.3	84.4
P700B	88.3	91.7	92.3	86.5
	2nd cycle	3rd cycle	4th cycle	5th cycle
P800A	144	149	140	145
P800B	115	114	114	114

[a]The carbonatation was conducted at 600, 700, and 800 °C under pure CO_2 flow. All tests were run in duplicate.

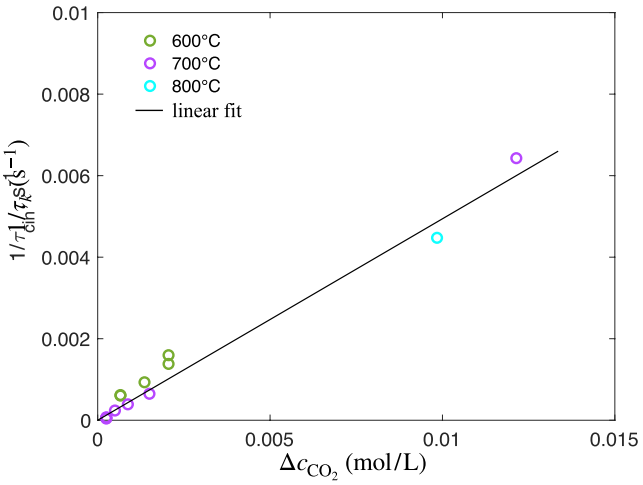

Figure 8. Inverse characteristic time at different values of the concentration distance from equilibrium conditions for isothermal single-carbonation TGA experiments. The linear scaling of each data set validates the kinetic expression postulated in eq 6. The fact that data at different temperatures are well correlated by a single linear fit implies that the kinetic constant k_s is essentially independent of the temperature in the interval considered.

cycles, as can be observed in Figure 9, where the values of $1/\tau_k$ vs Δc_{CO_2} determined from the five-cycle protocol data are reported. This peculiar behavior can be explained by assuming that physisorption on the reaction surface foregoes the actual chemical reaction so that the reacting species are CaO and CO_2 in the adsorbed state. In this case, the (Arrhenius-type) increase in the surface reaction constant with temperature could be mitigated by the reduction of the CO_2 concentration in the adsorbed state with increasing temperature due to thermodynamic effects associated with the exothermic nature of physisorption. Clearly, this is one of many possible explanations of this result, and tailored experiments should be devised to prove (or disprove) this mechanism.

Estimation of the Parameters Defining the Conversion-Dependent Diffusivity. Once the parameter τ_k has been computed from the early stages of the carbonatation as described above, eq 9 can be solved with respect to τ_D obtaining

$$\tau_D = \frac{1}{g(X_{CaO})}\left(\frac{1}{3}\frac{dX_{CaO}}{dt}(1 - X_{CaO})^{-2/3} - \tau_k\right) \quad (19)$$

https://doi.org/10.1021/acs.iecr.3c01820
Ind. Eng. Chem. Res. 2023, 62, 16647−16659

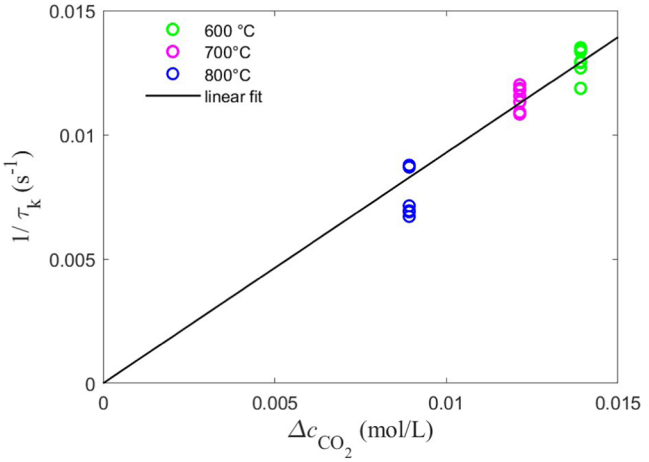

Figure 9. Inverse characteristic time at different temperatures for five-cycle protocol TGA experiments. The values of τ_k at each temperature refer to the second and subsequent carbonatation. The linear scaling of each data set validates the kinetic expression postulated in eq 6. The fact that data at different temperatures are well correlated by a single linear fit implies that the kinetic constant for the second and subsequent cycles is essentially independent of temperature in the interval considered.

The right-hand side of this equation can be computed from the TGA data, provided that a numerically accurate estimate of the conversion rate dX_{CaO}/dt is enforced. In what follows, a local quadratic interpolation to the set of experimental data is considered.

From this approach, the dependence of the characteristic time τ_D on the conversion is obtained from the experimental TGA data separately for the first and subsequent carbonatations. Figure 10 shows the trend of τ_D vs the second cycle carbonation conversion at different temperatures. From the values of τ_D determined for the second carbonatation and the subsequent ones, it is possible to obtain, through eq 11, the trend of the diffusion coefficient D_p as a function of τ_D at any given temperature

$$D_p(X_{CaO}) = \frac{1}{\tau_D(X_{CaO})} \frac{R_0^2}{\nu_{CaO}(c_{CO_2} - c_{CO_{2,eq}})} \quad (20)$$

As previously described in the Modeling section, an empirical expression (eq 8) is adopted to describe the diffusion coefficient dependency from conversion. The values D_p^0 and b are obtained by best fit of TGA data, linearizing eq 8

$$\log(D_p(X_{CaO})) = \log(D_p^0) + b \log(X_{CaO}) \quad (21)$$

The experimental data used to estimate the slope and the intercept of eq 21 refer to conversion trends as a function of time for higher conversion values (i.e., $X_{CaO} \geq 0.40-0.50$) when the CO_2 diffusion through the carbonate layer begins to have significant effects on the overall carbonation kinetics of the grain. In addition to conversion, the diffusion of CO_2 through the $CaCO_3$ layer is also influenced by temperature. Two different sets of values, one for the first cycle (Table 4)

Table 4. Values of D_p^0 and b to be Adopted in Equaion 8 for the Evaluation of $D_p(X_{CaO})$ during the First Carbonatation[a]

T (°C)	D_p^0 (m^2 s^{-1})	b
600	6.7×10^{-16}	5.51
700	7.8×10^{-16}	7.22
800	2.5×10^{-16}	8.86

[a]The parameters were separately estimated at 600, 700, and 800°C by best linear fit of first carbonatation TGA data collected at different CO2 compositions.

Table 5. Values of D_p^0 and b to be Adopted in eq 8 for the Evaluation of $D_p(X_{CaO})$ during the Second and Subsequent Carbonatation[a]

T (°C)	D_p^0 (m^2 s^{-1})	b
600	9.5×10^{-16}	4.7
700	3.2×10^{-16}	11.73
800	1.1×10^{-16}	18.71

[a]The parameters were separately estimated at 600, 700, and 800 °C by best linear fit of the second and subsequent cycle data of the five-cycle protocol, during which the carbonatation reaction was performed under a pure CO_2 flow.

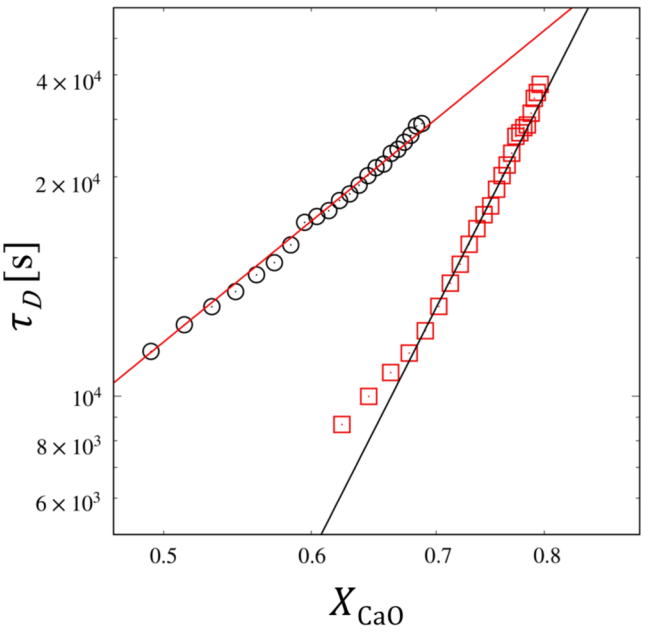

Figure 10. Scaling of τ_D with the second cycle carbonatation conversion at 700 °C (empty circles) and 800 °C (squares). In the log-norm representation of the figure, the parameters D_p^0 and b are obtained as the intercept and the slope of the best square fits represented by the continuous lines, respectively.

and the other for the subsequent cycles (Table 5), have been derived for D_p^0 and b, at any given temperature. In this regard, it is necessary to specify that, for the first carbonatation, which was carried out at different CO_2 compositions (see the Experimental Section), the values of D_p^0 and b reported in Table 5 were obtained by best linear fit of all TGA data collected at the same temperature, regardless of CO_2 compositions. As for the subsequent cycles, during which the reaction was conducted under a pure CO_2 flow, the parameters were estimated by best linear fit of the second to fifth carbonation data collected at any given temperature.

Estimate of τ_{cal}. The estimate of τ_{cal} can be obtained by fitting eq 18 to TGA calcination data by substituting $X_{CaCO_3}(t)$ and τ_{cal} in place of $X_{CaO}(t)$ and τ_k, respectively. Table 6 shows

https://doi.org/10.1021/acs.iecr.3c01820
Ind. Eng. Chem. Res. 2023, 62, 16647−16659

Table 6. Estimate of τ_{cal} and k_s' from Linear Regression of TGA Data for the Two-Cycle Calcination Protocol

T (°C)	τ_{cal} (s)	k_s' (mol s^{-1} m^{-2})
750	793	2.7
750	824	2.5
750	802	2.4
750	743	2.5
800	240	7.0
800	240	7.0
850	140	16.4
900	58	28.0
900	60	27.1

the values of k_s' as obtained by the two-cycle calcination experiments described in the Experimental Section. The data show that, unlike the kinetic constant of the carbonatation reaction k_s, the calcination constant k_s' does depend sensitively on temperature, as it undergoes a 10-fold increase when the temperature increases from 750 to 900 °C. The same table also reports the characteristic time τ_{cal} at different temperatures. As can be noted, this time becomes the order of several minutes when the temperature drops below 900 °C, thus suggesting that lower temperatures can hardly be enforced for the calcination process if a prompt response is sought (i.e., whenever the fluctuations of heat source to be shaved are characterized by high frequency). Figure 11 shows the

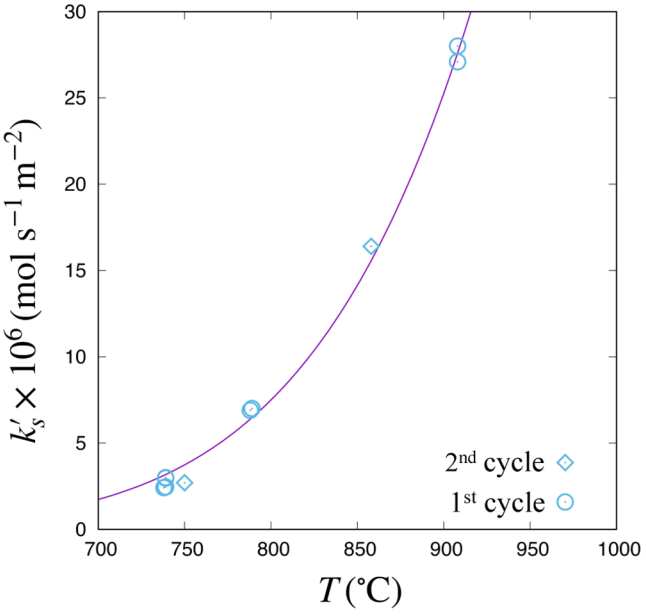

Figure 11. Arrhenius dependency of the calcination constant k_s' on temperature. Squares and circles represent data sets from different first and second calcination cycles, respectively.

nonlinear fit of k_s' with an Arrhenius-type dependency, $k_s'(T) = k_s'(T_0)\exp\left(-\frac{E_a}{R}\left(\frac{1}{T}-\frac{1}{T_0}\right)\right)$. The least-squares estimate yields $k_s'(1173\ \text{K}) = (25.2 \pm 0.4) \times 10^{-6}$ (mol m^{-2} s^{-1}) and $E_a/R = (15.393 \pm 0.49) \times 10^3$ K. It is worth observing that, contrary to the carbonatation, the kinetic constant for the calcination reaction can be assumed to be constant during the cycles for a fixed temperature of the gas feed.

Response under Looping: Experiments vs Model Predictions. The approaches described above are next applied to describe the behavior of the calcium oxide/mayenite material under carbonatation/calcination cycles. Figure 12

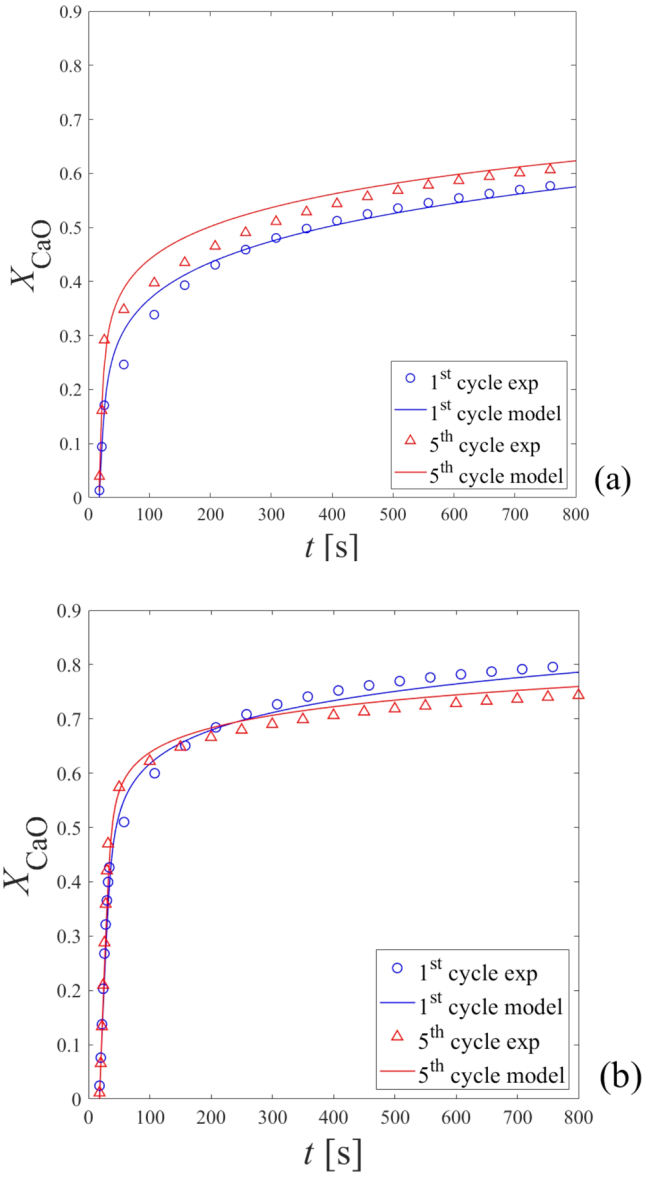

Figure 12. Comparison between model prediction and TGA data for a five-cycle calcium looping protocol. Panels (a) and (b) depict the carbonatation phase at 600 and 700 °C.

shows the comparison between theoretical predictions based on best fit parameters versus five-cycle protocol TGA experimental data. Panels (a) and (b) of the figure report the comparison for the first and fifth cycles for the carbonatation phase at T = 600 and 700 °C, respectively. Specifically, as previously explained in the Modeling section, in the generalized shrinking core model adopted for the first cycle, we assume that the external grain volume is not preserved. Conversely, the external volume grain is considered to remain constant for the second and subsequent cycles, with changes in the porosity during carbonatation and calcination. In this regard, as described in the previous sections, it is necessary to be precise that the kinetic/transport parameters, i.e., k_s, D_p^0, and b, adopted in the model for the first

https://doi.org/10.1021/acs.iecr.3c01820
Ind. Eng. Chem. Res. 2023, 62, 16647−16659

carbonatation, were computed separately from those referred to the second and subsequent carbonatations.

In Figure 12, one observes a significant difference between the first and fifth cycles, which is captured by the generalized shrinking core model provided that different sets of transport-reaction parameters are afforded. Specifically, model predictions appear adequately accurate in the pure regimes (kinetic- and diffusion-dominated which are associated with the short- and long-time behaviors of the conversion curves, respectively), whereas a certain discrepancy can be observed at intermediate times when the regime switch occurs.

In conclusion, the modeling approach developed in this article provides a robust estimate of the behavior of micrometric CaO−mayenite particles under looping.

CONCLUSIONS

A wealth of studies available in the literature have investigated the use of CaO/mayenite-based materials for CO_2-capture processes. Besides, economic, safety, and stability considerations suggest that CaO/mayenite particles may prove a viable material for thermochemical storage looping processes, where the material is subject to repeated cycles of carbonatation/calcination reactions. In this study, a characterization of the material for CaO/$CaCO_3$ looping is carried out by interpreting TGA data through a generalized shrinking core model enforcing a conversion-dependent effective diffusion coefficient for the transport of CO_2 within the particle pores. A thermodynamic-consistent first-order kinetics ($-r_{CaO}$) is postulated and verified by linear regression of TGA data at the early stages of the carbonatation reaction. The data fitting validates the kinetic expression in a temperature range of 200 °C. Interestingly, the kinetic constant appears weakly dependent on temperature in this range, a phenomenon that may be justified by a physisorption-surface reaction sequence. Based on previous studies on similar materials, a two-parameter conversion-dependent diffusion coefficient for CO_2 is considered to model the transport of CO_2 inside the pores. Linear regression on TGA data is used to estimate the diffusivity parameters, showing that the conversion-dependent diffusion model is consistent with experimental results.

Due to the overpressure associated with CO_2 release during the calcination phase, which triggers convective flow facilitating the exit of the gas from the porous grain, a purely kinetic model is used to describe this phase of the cycle. Best fit of TGA data proves that, unlike the case of the carbonatation, the calcination kinetic constant depends sensitively on temperature.

The kinetic and transport expression being established for both reactions, carbonatation/calcination cycles were enforced in order to test the performance of the material over looping. Significant differences were found between the kinetic constant and diffusion coefficient associated with the first cycle (starting with virgin nonporous CaO/mayenite particles) and those of subsequent cycles, which resulted in being essentially constant over cycling. Thus, separate constants were computed from the first and the second carbonations, and based on this, a five-looping protocol was predicted based on the generalized shrinking core model. A good agreement with the experimental TGA results was found.

The natural follow-up of this research is to use the information about the single CaO/mayenite grain discussed here to build up a model for the chemical reactor operating at the industrial scale, where additional mass and energy transport time scales are introduced depending on the reactor type (fluidized vs fixed bed) and size. In this respect, the parameters k_s, D_p^0, and b could serve to fix the target conversion under kinetic control, which should be considered as an upper bound for obtaining a fast reactor response.

AUTHOR INFORMATION

Corresponding Author

Maria Anna Murmura − *Dipartimento di Ingegneria Chimica Materiali Ambiente, Sapienza Università di Roma, 00184 Roma, Italy;* orcid.org/0000-0001-8741-0552; Email: mariaanna.murmura@uniroma1.it

Authors

Silvia Lo Conte − *Dipartimento di Ingegneria Chimica Materiali Ambiente, Sapienza Università di Roma, 00184 Roma, Italy*

Francesca Fratini − *Dipartimento di Ingegneria Chimica Materiali Ambiente, Sapienza Università di Roma, 00184 Roma, Italy*

Stefano Cerbelli − *Dipartimento di Ingegneria Chimica Materiali Ambiente, Sapienza Università di Roma, 00184 Roma, Italy;* orcid.org/0000-0003-3906-6595

Michela Lanchi − *Energy and Sustainable Economic Development, ENEA - Italian National Agency for New Technologies, 00123 Rome, Italy*

Annarita Spadoni − *Energy and Sustainable Economic Development, ENEA - Italian National Agency for New Technologies, 00123 Rome, Italy*

Luca Turchetti − *Energy and Sustainable Economic Development, ENEA - Italian National Agency for New Technologies, 00123 Rome, Italy*

Maria Cristina Annesini − *Dipartimento di Ingegneria Chimica Materiali Ambiente, Sapienza Università di Roma, 00184 Roma, Italy;* orcid.org/0000-0002-4624-7661

Complete contact information is available at: https://pubs.acs.org/10.1021/acs.iecr.3c01820

Notes

The authors declare no competing financial interest.

ACKNOWLEDGMENTS

This work was funded by the Italian Ministry of Ecological Transition through Ricerca di Sistema Elettrico Nazionale (RdS), the "National Electricity System Research" program 2019−2021 triennial implementation plan—Project 1.2.

REFERENCES

(1) *Renewable Electricity*; International Energy Agency, 2022.

(2) *World Energy Outlook 2019*; International Energy Agency, 2019.

(3) *EASE-EERA Energy Storage Technology Development Roadmap 2017*; European Association of Storage Energy, 2017.

(4) European Environment Agency (EEA). http://www.eea.europa.eu/.

(5) Miró, L.; Brückner, S.; Cabeza, L. F. Mapping and discussing Industrial Waste Heat (IWH) potentials for different countries. *Renewable Sustainable Energy Rev.* **2015**, *51*, 847−855.

(6) Brueckner, S.; Miró, L.; Cabeza, L. F.; Pehnt, M.; Laevemann, E. Methods to estimate the industrial waste heat potential of regions − A categorization and literature review. *Renewable Sustainable Energy Rev.* **2014**, *38*, 164−171.

(7) Bailera, M.; Pascual, S.; Lisbona, P.; Romeo, L. M. Modelling calcium looping at industrial scale for energy storage in concentrating solar power plants. *Energy* **2021**, *225*, 120306.

(8) Gil, A.; Medrano, M.; Martorell, I.; Lázaro, A.; Dolado, P.; Zalba, B.; Cabeza, L. F. State of the art on high temperature thermal energy storage for power generation. Part 1—Concepts, materials and modellization. *Renewable Sustainable Energy Rev.* **2010**, *14*, 31−55.
(9) Bayon, A.; Bader, R.; Jafarian, M.; Fedunik-Hofman, L.; Sun, Y.; Hinkley, J.; Miller, S.; Lipiński, W. Techno-economic assessment of solid−gas thermochemical energy storage systems for solar thermal power applications. *Energy* **2018**, *149*, 473−484.
(10) Liu, M.; Tay, N. S.; Bell, S.; Belusko, M.; Jacob, R.; Will, G.; Saman, W.; Bruno, F. Review on concentrating solar power plants and new developments in high temperature thermal energy storage technologies. *Renewable Sustainable Energy Rev.* **2016**, *53*, 1411−1432.
(11) Pardo, P.; Deydier, A.; Anxionnaz-Minvielle, Z.; Rougé, S.; Cabassud, M.; Cognet, P. A review on high temperature thermochemical heat energy storage. *Renewable Sustainable Energy Rev.* **2014**, *32*, 591−610.
(12) Lanchi, M.; Turchetti, L.; Sau, S.; Liberatore, R.; Cerbelli, S.; Murmura, M. A.; Annesini, M. C. A Discussion of Possible Approaches to the Integration of Thermochemical Storage Systems in Concentrating Solar Power Plants. *Energies* **2020**, *13*, 4940.
(13) Prasad, J. S.; Muthukumar, P.; Desai, F.; Basu, D. N.; Rahman, M. M. A critical review of high-temperature reversible thermochemical energy storage systems. *Applied Energy* **2019**, *254*, No. 113733.
(14) Han, X.; Wang, L.; Ling, H.; Ge, Z.; Lin, X.; Dai, X.; Chen, H. Critical review of thermochemical energy storage systems based on cobalt, manganese, and copper oxides. *Renewables Sustainable Energy Rev.* **2022**, *158*, No. 112076.
(15) Ortiz, C.; Valverde, J.; Chacartegui, R.; Perez-Maqueda, L.; Giménez, P. The Calcium-Looping (CaCO3/CaO) process for thermochemical energy storage in Concentrating Solar Power plants. *Renewable Sustainable Energy Rev.* **2019**, *113*, No. 109252.
(16) Salaudeen, S. A.; Acharya, B.; Dutta, A. CaO-based CO2 sorbents: A review on screening, enhancement, cyclic stability, regeneration and kinetics modelling. *J. CO2 Util.* **2018**, *23*, 179−199.
(17) Abanades, J. C.; Alvarez, D. Conversion Limits in the Reaction of CO2 with Lime. *Energy Fuels* **2003**, *17*, 308−315.
(18) Alvarez, D.; Abanades, J. C. Determination of the Critical Product Layer Thickness in the Reaction of CaO with CO2. *Ind. Eng. Chem. Res.* **2005**, *44*, 5608−5615.
(19) Bhatia, S. K.; Perlmutter, D. D. A random pore model for fluid-solid reactions: II. Diffusion and transport effects. *AIChE J.* **1981**, *27*, 247−254.
(20) Bhatia, S. K.; Perlmutter, D. D. Effect of the product layer on the kinetics of the CO2-lime reaction. *AIChE J.* **1983**, *29*, 79−86.
(21) Liu, W.; González, B.; Dunstan, M. T.; Sultan, D. S.; Pavan, A.; Ling, C. D.; Grey, C. P.; Dennis, J. Structural evolution in synthetic, Ca-based sorbents for carbon capture. *Chem. Eng. Sci.* **2016**, *139*, 15−26.
(22) Stendardo, S.; Foscolo, P. U. Carbon dioxide capture with dolomite: A model for gas−solid reaction within the grains of a particulate sorbent. *Chemical Engineering Science* **2009**, *64*, 2343−2352.
(23) Sarrión, B.; Perejón, A.; Sánchez-Jiménez, P. E.; Pérez-Maqueda, L. A.; Valverde, J. M. Role of calcium looping conditions on the performance of natural and synthetic Ca-based materials for energy storage. *J. CO2 Util.* **2018**, *28*, 374−384.
(24) Fennell, P. S.; Pacciani, R.; Dennis, J. S.; Davidson, J. F.; Hayhurst, A. N. The Effects of Repeated Cycles of Calcination and Carbonation on a Variety of Different Limestones, as Measured in a Hot Fluidized Bed of Sand. *Energy Fuels* **2007**, *21*, 2072−2081.
(25) Grasa, G. S.; Abanades, J. C. CO2 Capture Capacity of CaO in Long Series of Carbonation/Calcination Cycles. *Ind. Eng. Chem. Res.* **2006**, *45*, 8846−8851.
(26) Valverde, J. M.; Sanchez-Jimenez, P. E.; Perejon, A.; Perez-Maqueda, L. A. Role of Looping-Calcination Conditions on Self-Reactivation of Thermally Pretreated CO2 Sorbents Based on CaO. *Energy Fuels* **2013**, *27*, 3373−3384.
(27) Benitez-Guerrero, M.; Sarrion, B.; Perejon, A.; Sanchez-Jimenez, P. E.; Perez-Maqueda, L. A.; Manuel Valverde, J. Large-scale high-temperature solar energy storage using natural minerals. *Sol. Energy Mater. Sol. Cells* **2017**, *168*, 14−21.
(28) Al-Mamoori, A.; Lawson, S.; Rownaghi, A. A.; Rezaei, F. Improving Adsorptive Performance of CaO for High-Temperature CO2 Capture through Fe and Ga Doping. *Energy Fuels* **2019**, *33*, 1404−1413.
(29) Azimi, B.; Tahmasebpoor, M.; Sanchez-Jimenez, P. E.; Perejon, A.; Valverde, J. M. Multicycle CO2 capture activity and fluidizability of Al-based synthesized CaO sorbents. *Chem. Eng. J.* **2019**, *358*, 679−690.
(30) Sun, J.; Yang, Y.; Guo, Y.; Zhao, C.; Zhang, J.; Liu, W.; Lu, P. Stabilized Performance of Al-Decorated and Al/Mg Co-Decorated Spray-Dried CaO-Based CO2 Sorbents. *Chem. Eng. Technol.* **2019**, *42*, 1283−1292.
(31) Radfarnia, H. R.; Iliuta, M. C. Metal oxide-stabilized calcium oxide CO2 sorbent for multicycle operation. *Chem. Eng. J.* **2013**, *232*, 280−289.
(32) Lanchi, M.; Spadoni, A.; Sau, S.; Tizzoni, A. C.; Varsano, F.; Corsaro, N.; Turchetti, L.; Liberatore, R.; Mauro, A. D. G. D.; Delise, T.; Mansi, E.; Murmura, M. A.; Annesini, M. C. Mayenite-supported CaO for thermochemical storage applications: Ageing time effect over conversion. *AIP Conf. Proc.* **2022**, *2445*, No. 160009.
(33) Sau, S.; Varsano, F.; Tizzoni, A. C.; Corsaro, N.; Frittella, C.; Lanchi, M.; Liberatore, R.; Spadoni, A.; Turchetti, L.; Annesini, M. C. Mayenite-supported CaO for thermochemical storage applications: Analysis of dynamic behavior under charging/discharging cycles. *AIP Conf. Proc.* **2020**, *2303*, No. 200005.
(34) Materić, V.; Symonds, R.; Lu, D.; Holt, R.; Manović, V. Performance of Hydration Reactivated Ca Looping Sorbents in a Pilot-Scale, Oxy-fired Dual Fluid Bed Unit. *Energy Fuels* **2014**, *28*, 5363−5372.
(35) Coppola, A.; Salatino, P.; Montagnaro, F.; Scala, F. Reactivation by water hydration of the CO2 capture capacity of a calcium looping sorbent. *Fuel* **2014**, *127*, 109−115.
(36) Champagne, S.; Lu, D. Y.; Macchi, A.; Symonds, R. T.; Anthony, E. J. Influence of Steam Injection during Calcination on the Reactivity of CaO-Based Sorbent for Carbon Capture. *Ind. Eng. Chem. Res.* **2013**, *52*, 2241−2246.
(37) Lu, H.; Smirniotis, P. G.; Ernst, F. O.; Pratsinis, S. E. Nanostructured Ca-based sorbents with high CO2 uptake efficiency. *Chem. Eng. Sci.* **2009**, *64*, 1936−1943.
(38) Florin, N. H.; Harris, A. T. Reactivity of CaO derived from nano-sized CaCO3 particles through multiple CO2 capture-and-release cycles. *Chem. Eng. Sci.* **2009**, *64*, 187−191.
(39) Hu, Y.; Liu, W.; Sun, J.; Li, M.; Yang, X.; Zhang, Y.; Liu, X.; Xu, M. Structurally improved CaO-based sorbent by organic acids for high temperature CO2 capture. *Fuel* **2016**, *167*, 17−24.
(40) Benitez-Guerrero, M.; Valverde, J. M.; Perejon, A.; Sanchez-Jimenez, P. E.; Perez-Maqueda, L. A. Effect of milling mechanism on the CO2 capture performance of limestone in the Calcium Looping process. *Chem. Eng. J.* **2018**, *346*, 549−556.
(41) Tian, X.; Lin, S.; Yan, J.; Zhao, C. Sintering mechanism of calcium oxide/calcium carbonate during thermochemical heat storage process. *Chem. Eng. J.* **2022**, *428*, 131229.
(42) Yang, L.; Huang, G.; Huang, Z. Optimized design of Ca-based thermochemical heat storage materials for concentrated solar power. *J. Energy Storage* **2021**, *43*, No. 103236, DOI: 10.1016/j.est.2021.103236.
(43) Muto, A.; McCabe, K.; Real, D. High-temperature calcium-based thermochemical energy storage system for use with CSP facilities. *AIP Conf. Proc.* **2018**, No. 100006, DOI: 10.1063/1.5067127.
(44) Martavaltzi, C. S.; Lemonidou, A. Parametric Study of the CaO $Ca_{12}Al_{14}O_{33}$ Synthesis with Respect to High CO2 Sorption Capacity and Stability on Multicycle Operation. *Ind. Eng. Chem. Res.* **2008**, *47*, 9537−9543.
(45) Di Giuliano, A.; Gallucci, K.; Foscolo, P. U. Determination of kinetic and diffusion parameters needed to predict the behavior of

CaO-based CO2 sorbent and sorbent-catalyst materials. *Ind. Eng. Chem. Res.* **2020**, *59*, 6840−6854.
(46) Li, Z.-s.; Cai, N.-s.; Huang, Y.-y.; Han, H.-j. Synthesis, experimental studies, and analysis of a new calcium-based carbon dioxide absorbent. *Energy Fuels* **2005**, *19*, 1447−1452.
(47) Spadoni, A.; Sau, S.; Corsaro, N.; Lanchi, M.; Tizzoni, A.; Veca, E.; Falconieri, M.; Della Seta, L.; Del Mauro, A. D. G.; Turchetti, L.; et al. Thermochemical heat storage through CaO-Mayenite/CaCO3 system: Thermal performances comparison for two synthesis methods. *J. Energy Storage* **2023**, *72*, No. 108386.
(48) Di Giuliano, A.; Girr, J.; Massacesi, R.; Gallucci, K.; Courson, C. Sorption enhanced steam methane reforming by Ni−CaO materials supported on mayenite. *Int. J. Hydrogen Energy* **2017**, *42*, 13661−13680.
(49) García-Labiano, F.; Abad, A.; de Diego, L. F.; Gayán, P.; Adánez, J. Calcination of calcium-based sorbents at pressure in a broad range of CO2 concentrations. *Chem. Eng. Sci.* **2002**, *57*, 2381−2393.
(50) Escardino, A.; García-Ten, J.; Feliu, C.; Saburit, A.; Cantavella, V. Kinetic study of the thermal decomposition process of calcite particles in air and CO2 atm. *J. Ind. Eng. Chem.* **2013**, *19*, 886−897.
(51) Campbell, F. R.; Hills, A. W. D.; Paulin, A. Transport properties of porous lime and their influence on the decomposition of porous compacts of calcium carbonate. *Chem. Eng. Sci.* **1970**, *25*, 929−942.

https://doi.org/10.1021/acs.iecr.3c01820
Ind. Eng. Chem. Res. 2023, 62, 16647−16659